



Modelling and simulation of natural hydraulic fracturing applied to experiments on natural sandstone cores

Junxiang Wang¹ · Alixa Sonntag² · Dongwon Lee² · Giovanna Xotta¹ · Valentina A. Salomoni³ · Holger Steeb² · Arndt Wagner² · Wolfgang Ehlers²

Received: 15 September 2023 / Accepted: 7 May 2024
© The Author(s) 2024

Abstract

Under in-situ conditions, natural hydraulic fractures (NHF) can occur in permeable rock structures as a result of a rapid decrease of pore water accompanied by a local pressure regression. Obviously, these phenomena are of great interest for the geo-engineering community, as for instance in the framework of mining technologies. Compared to induced hydraulic fractures, NHF do not evolve under an increasing pore pressure resulting from pressing a fracking fluid in the underground but occur and evolve under local pore-pressure reductions resulting in tensile stresses in the rock material. The present contribution concerns the question under what quantitative circumstances NHF emerge and evolve. By this means, the novelty of this article results from the combination of numerical investigations based on the Theory of Porous Media with a tailored experimental protocol applied to saturated porous sandstone cylinders. The numerical investigations include both pre-existing and evolving fractures described by use of an embedded phase-field fracture model. Based on this procedure, representative mechanical and hydraulic loading scenarios are simulated that are in line with experimental investigations on low-permeable sandstone cylinders accomplished in the Porous Media Lab of the University of Stuttgart. The values of two parameters, the hydraulic conductivity of the sandstone and the critical energy release rate of the fracture model, have turned out essential for the occurrence of tensile fractures in the sandstone cores, where the latter is quantitatively estimated by a comparison of experimental and numerical results. This parameter can be taken as reference for further studies of in-situ NHF phenomena and experimental results.

Keywords Crack resistance · Hydraulic conductivity · Hydraulic fracturing · Phase-field method · Porous sandstone · Theory of Porous Media

1 Introduction

Hydraulically induced fracturing in porous media can be divided into two main categories, namely induced hydraulic fracturing (IHF) and natural hydraulic fracturing (NHF). In the field of geo-engineering, IHF is frequently

used to make the underground suitable for resource extraction or final storage. Therefore, cracks and fissures are artificially induced (stimulated) through the injection of a fluid under high pressure, commonly known as fracking, cf., e. g., the review article of Chen et al. [11] and citations therein.

Another hydraulic fracturing phenomenon occurs frequently in practise, when the in-situ equilibrium conditions (natural mechanical and hydraulic loading conditions) change in a porous rock formation. For example, this is the case when the steady-state flow of deep groundwater within sandstone is affected by a variation of the total external loading pressure, e. g. due to tunnelling or drilling. As a result of the interaction between the components of a fluid-saturated porous material, effective tensile stresses are generated within the solid skeleton in order to adapt to the

✉ Arndt Wagner
arndt.wagner@mechbau.uni-stuttgart.de

¹ Department of Civil, Environmental and Architectural Engineering, University of Padua, Via Francesco Marzolo 9, 35121 Padua, Italy

² University of Stuttgart, Institute of Applied Mechanics, Pfaffenwaldring 7, 70569 Stuttgart, Germany

³ Department of Management and Engineering, University of Padua, Stradella S. Nicola 3, 36100 Vicenza, Italy

changed boundary conditions. This effect can result in fracturing processes within the porous rock, known as NHF. In contrast to IHF, the driving force for NHF is not the increasing pore pressure. Instead, the newly created cracks allow water to flow in to fill them up, which decreases pore pressure, thus also inducing tensile rock stresses.

For the description of IHF, a variety of different methods can be found in the literature. Shauer and Duarte [41] adopted the generalised finite element method (GFEM), Lecampion [31] employed the extended finite element method (XFEM), and Yi et al. [48] proposed a coupled fluid-flow and rock-damage model to describe fracture propagation in rock under consideration of a fluid injection rate, viscosity and confining far-field stresses. Moreover, Nguyen et al. [39] presented a cohesive interface element method.

In recent years, the usage of multiphasic models with an embedded phase-field approach to model brittle fracture received more attention, cf., e. g., Mikelić et al. [37], Heider and Markert [25] or Ehlers and Luo [17, 18], just to name a few. While the above articles describe fully saturated media, Sonntag et al. [42] expanded these findings to a fully coupled analysis of partially saturated media. Apart from brittle fracture, the phase-field method was also applied to ductile fracture for single-phasic materials, e. g., in Ambati et al. [2], Borden et al. [7] or Miehe et al. [35]. A systematic review of model approaches for flow in fractured porous media has been presented by Berre et al. [4, 5] based on benchmark problems. Furthermore, comprehensive reviews for modelling IHF can be found in, e. g., Lecampion et al. [32], Davies et al. [14], Adachi et al. [1] or Chen et al. [11].

Current research regarding NHF mainly focuses on already existing natural cracks and their interaction with IHF but do not study their origin. In this regard, Kolawole and Ispas [29] reported a comprehensive literature review on the interaction between IHF and NHF. Therein, the authors state that numerical modelling and simulation is applied more often than experimental approaches, and analytical methods are used the least. Obviously, pre-existing natural fractures influence IHF and result in various effects, such as turning, kinking, branching and coalescing. To describe these effects, several models were presented. For example, Cordero et al. [12] adopted cohesive interface elements, Zheng et al. [51] presented a model based on XFEM, Yi et al. [49] proposed a new fluid flow model and Zhang et al. [50] carried out a fully coupled numerical analysis, based on the concept of synthetic rock-mass modelling (SRM) to investigate the fluid-driven fracture in naturally fractured rocks. A field study in soft coal seams was carried out by Lyu et al. [34], Liu et al. [33] designed an experimental model and Gale et al. [23] performed a

detailed analysis of NHF on a test site, including their orientation, size, spatial distribution and openness.

However, all of these studies basically assume already existing and static (non-evolving) NHF. Therefore, they are beneficial to improve the understanding of the behaviour of NHF and their influence on IHF but neglect the question of what happened before, namely why NHF occur and how NHF develop in situ. Due to the limited research on this aspect, modelling NHF represents a current and partly open research topic. Therefore, these questions are focused in this contribution using a combined investigation of numerical simulations and experiments. Modelling NHF implies to account for the coupled multiphasic material behaviour of the solid and fluid components as well as for the inclusion of a fracture model to describe the occurrence and evolution of NHF processes within the multiphasic material.

While numerous qualitative studies have been carried out on IHF and on the interaction between NHF and IHF, only little research has been accomplished so far to answer the question under what quantitative circumstances NHF emerge and evolve. By this means, the novelty of this article results from the combination of numerical investigations based on of the Theory of Porous Media (TPM) with a tailored experimental protocol applied to saturated porous sandstone cylinders. In particular, these investigations are based on modelling NHF in sedimentary sandstone rocks (Anröchter sandstone) both theoretically and numerically by enhancing the TPM through the phase-field approach to fracture. Therefore, an experimental setup for fully water-saturated sandstone cores under hydraulically induced pressure conditions combined with mechanically applied triaxial external loading conditions has been investigated at the Porous Media Lab (PML) of the University of Stuttgart. These experimental hydraulic fracturing procedures are then studied by accompanying simulations: (i) a classical biphasic model in the framework of the TPM and (ii) the same model with an embedded phase-field approach to fracture. Using (i), we evaluate the stress and pressure distributions occurring during the experimental investigations. After the basic behaviour is described we further use (ii) to justify the failure criteria and estimate material parameters of the TPM phase-field model.

The manuscript is organised as follows. Chapter 2 introduces the basic framework of the TPM (Sect. 2.1) and the embedded phase-field approach to fracture (Sect. 2.2) allowing to model NHF. Chapter 3 presents the experimental setup for NHF in sandstone cores. Therein, the experimental investigations are introduced in detail. Based on the experiments, Chapter 4 presents the numerical examples of the considered fully saturated sandstone cores under controlled triaxial stress conditions. In particular, a

detailed study of the stress distribution for the involved components without a consideration of a crack evolution is first given in Sect. 4.1. Therein, special attention is paid to the principal generation of effective tensile stresses in the solid skeleton under the experimental loading protocol. Then the TPM-phase-field model is used in Sect. 4.2 to simulate the occurrence and evolution of NHF. Therein, a specific focus is laid in Sect. 4.2.1 on the influence of the critical crack resistance and in Sect. 4.2.2 on the influence of the hydraulic conductivity (Darcy permeability) on the fracturing behaviour. Moreover, several cases are investigated in Sect. 4.2.3 in detail, showing different possibilities of evolving fracture profiles. These cases are compared with each other and related to the experimental results. Finally, Chapter 5 gives the conclusions and future research perspectives.

2 Modelling approach

The considerations above motivate the usage of a multiphase modelling approach to meaningfully describe the coupled processes in dense porous rocks. In this chapter, the fundamentals of the basic biphasic TPM model and its combination with the phase-field approach to fracture to obtain an embedded TPM-phase-field method are briefly presented based on referenced literature.

2.1 Biphasic TPM model

Several approaches can be found for a continuum-mechanical description of the coupled processes occurring in multiphase (porous) media, e. g., the Biot theory [6], poroelastic approaches [13, 43] or the theory of porous media (TPM) [15, 16], just to name a few. In this work, the TPM is favoured based on the following arguments. Since the TPM evolved from the theory of mixtures, which goes back to Truesdell and Toupin [44], Bowen [9, 10] and many others, this approach is based on first principles of rational thermodynamics. Therefore, the TPM allows for a rigorous and consistent model formulation. The concept of a virtual smearing (volumetric averaging) of the real pore morphology on the microscale yields a macroscopic model of superimposed and interacting continua. This means that each constituent owns an individual motion function as a basis for a continuum-mechanical description, and balance equations. The individual balance equations of the different constituents are coupled to each other via so-called production terms, e. g., mass or momentum exchange between the constituents.

The basic biphasic TPM model has been established decades ago and is therefore only briefly summarised here for the sake of completeness, cf., e. g., Ehlers [16] or

Ehlers and Wagner [19]. The overall macroscopic model φ of superimposed and interacting continua is composed of a materially incompressible solid skeleton φ^S and a materially incompressible pore liquid φ^L , viz.:

$$\varphi = \bigcup_{\alpha} \varphi^{\alpha} = \varphi^S \cup \varphi^L \quad \text{with } \alpha = \{S, L\}. \quad (1)$$

As basic quantities to express the volumetric composition of the porous medium, volume fractions are classically defined via $n^{\alpha} := dv^{\alpha}/dv$ with $n^S + n^L = 1$, where the sum of the volume fractions equals always one, thus describing the so-called saturation condition. Furthermore, two different density functions are introduced, the real density $\rho^{\alpha R} := dm^{\alpha}/dv^{\alpha}$ and the partial density $\rho^{\alpha} := dm^{\alpha}/dv$. Since the local mass element dm^{α} is related in the latter case to the bulk volume element dv of the so-called representative elementary volume (REV), the partial density can be interpreted as a volumetrically averaged density on the macroscale, which is also seen by the relation $\rho^{\alpha} = n^{\alpha} \rho^{\alpha R}$.

In an isothermal environment, the specific balance equations of immiscible constituents are given by the mass and momentum balances, viz.:

$$\begin{aligned} (\rho^{\alpha})'_{\alpha} + \rho^{\alpha} \operatorname{div} \dot{\mathbf{x}}_{\alpha} &= 0 \quad \text{and} \\ \rho^{\alpha} \ddot{\mathbf{x}}_{\alpha} &= \operatorname{div} \mathbf{T}^{\alpha} + \rho^{\alpha} \mathbf{g} + \hat{\mathbf{p}}^{\alpha}. \end{aligned} \quad (2)$$

Therein, $\hat{\mathbf{p}}^{\alpha}$ is the direct momentum production term of the constituent φ^{α} , \mathbf{T}^{α} defines the partial Cauchy stress tensor of φ^{α} , and \mathbf{g} is the gravitation vector. In (2), $\dot{\mathbf{x}}_{\alpha}$ and $\ddot{\mathbf{x}}_{\alpha}$ are the velocity and acceleration of φ^{α} , while $(\cdot)'_{\alpha}$ is the material time derivative following the motion of φ^{α} . Note that the assumption of materially incompressible materials with constant real density $\rho^{\alpha R}$ results in volume balances

$$(n^{\alpha})'_{\alpha} + n^{\alpha} \operatorname{div} \dot{\mathbf{x}}_{\alpha} = 0. \quad (3)$$

For a saturated porous medium with incompressible constituents, the volume balance of the overall aggregate reads

$$n^S \operatorname{div} \dot{\mathbf{x}}_S + n^F \operatorname{div} \dot{\mathbf{x}}_F + \operatorname{grad} n^F \cdot \mathbf{w}_F = 0. \quad (4)$$

Therein, $\mathbf{w}_F := \dot{\mathbf{x}}_F - \dot{\mathbf{x}}_S$ is the seepage velocity. To ensure that the constitutive equations for the stresses and the production terms are thermodynamically admissible, they have to fulfil the entropy inequality. Therefore, the constitutive choice of the Helmholtz free energies $\psi^S = \psi^S(\mathbf{F}_S)$ with \mathbf{F}_S as the solid deformation gradient and $\psi^L = \psi^L(-)$ has been made. Neglecting gravitational effects ($\mathbf{g} = \mathbf{0}$), this leads to the following constitutive equations:

$$\begin{aligned} \mathbf{T}^\alpha &= \mathbf{T}_E^\alpha - n^\alpha p \mathbf{I}, & \hat{\mathbf{p}}^L &= p \operatorname{grad} n^L + \hat{\mathbf{p}}_E^L, \\ \mathbf{T}_E^S &= \rho^S \frac{\partial \psi^S}{\partial \mathbf{F}_S} \mathbf{F}_S^T \approx \boldsymbol{\sigma}_E^S = 2\mu^S \boldsymbol{\varepsilon}_S + \lambda^S (\boldsymbol{\varepsilon}_S \cdot \mathbf{I}) \mathbf{I}, & (5) \\ \hat{\mathbf{p}}_E^L &= -\frac{(n^L)^2 \mu^{LR}}{K^S} \mathbf{w}_L \rightarrow n^L \mathbf{w}_L = -\frac{K^S}{\mu^{LR}} \operatorname{grad} p, \end{aligned}$$

where p denotes the pore pressure and \mathbf{I} the second-order identity tensor. For the effective stress of the solid, \mathbf{T}_E^S , with $\boldsymbol{\sigma}_E^S$ as its linearised counterpart, the linear elastic (Hookean) approach with the Lamé constants μ^S and λ^S has been applied, where $\boldsymbol{\varepsilon}_S = \frac{1}{2}(\operatorname{grad} \mathbf{u}_S + \operatorname{grad}^T \mathbf{u}_S)$ is the linearised solid strain tensor based on the gradient of the solid displacement vector \mathbf{u}_S . Summing up the momentum balances (2)₂ under the assumption of quasi-static conditions yields the overall momentum balance (6)₁, where the total stress $\mathbf{T} = \mathbf{T}^S + \mathbf{T}^L = \mathbf{T}_E^S - p \mathbf{I}$ is found by applying the principle of effective stresses as well as by neglecting the liquid extra stresses. In (5)₃, a standard Darcy filter law is obtained from the momentum balance of the liquid. Therein, K^S is the intrinsic permeability and μ^{LR} the effective dynamic viscosity of the liquid. The intrinsic permeability $K^S = \mu^{LR} k^L / (\rho^{LR} g)$ depends only on the pore morphology of the solid, whereas the Darcy permeability (hydraulic conductivity) k^L also depends on the fluid properties and the gravitation $g = |\mathbf{g}|$. Inserting Darcy's filter law into the overall volume balance (4) yields the second governing equation assigned to the pore pressure p , acting as the second primary variable. In conclusion, the set of coupled partial differential equations is found under quasi-static conditions as:

$$\begin{aligned} \mathbf{0} &= \operatorname{div} \mathbf{T}_E^S - \operatorname{grad} p, \\ 0 &= \operatorname{div}[(\mathbf{u}_S)'_S - \frac{K^S}{\mu^{LR}} \operatorname{grad} p]. \end{aligned} \quad (6)$$

For further discussion, the interested reader is referred to, e. g., Ehlers [16].

2.2 Biphasic TPM model with embedded phase-field approach to fracture

In this subsection, the description of the basic multiphase material behaviour introduced in Sect. 2.1 is enriched by a diffuse fracture description using the well-suited phase-field approach. In particular, the original model of Ehlers and Luo [17, 18] is used for the description of brittle dynamic hydraulic fracturing in fully-saturated porous media. This model is briefly summarised here to provide an overview. For more background, the interested reader is referred to fundamental works, e. g., Griffith [24], Francfort and Marigo [21] and Miehe et al. [36] or to the review article of Ambati et al. [3] for quasi-static and dynamic

phase-field modelling of brittle fracture in single-phasic materials.

The principle for incorporating a phase-field approach within the TPM is to extend the set of process variables for the solid's free energy by integrating the phase-field variable

$$\begin{aligned} \phi^S(\mathbf{x}, t) &\in [0, 1] \\ \text{with } \begin{cases} \phi^S = 0 & : \text{intact solid phase,} \\ 0 < \phi^S < 1 & : \text{diffuse interface,} \\ \phi^S = 1 & : \text{fully broken solid phase,} \end{cases} \end{aligned} \quad (7)$$

and its gradient $\operatorname{grad} \phi^S$ via $\psi^S = \psi^S(\boldsymbol{\varepsilon}_S, \phi^S, \operatorname{grad} \phi^S)$, where $\boldsymbol{\varepsilon}_S = \frac{1}{2}(\mathbf{F}_S + \mathbf{F}_S^T) - \mathbf{I}$ substitutes \mathbf{F}_S . In comparison to Sect. 2.1, the standard constitutive choice of ψ^S for fully saturated porous media is extended for the consideration of fracturing processes therein. In this regard, we further restrict our considerations to a small-strain approach of the porous solid. Further restrictions for a thermodynamically consistent constitutive setting are obtained by the evaluation of the entropy inequality (Coleman-Noll procedure) as described in Ehlers and Luo [17], yielding

$$\boldsymbol{\sigma}_E^S = \rho_0^S \frac{\partial \psi^S}{\partial \boldsymbol{\varepsilon}_S} \quad \text{and} \quad \operatorname{div} \left((\phi^S)'_S \rho_0^S \frac{\partial \psi^S}{\partial \operatorname{grad} \phi^S} \right) = 0, \quad (8)$$

where $\rho_0^S = \rho^S \det \mathbf{F}_S$ is the partial solid density in the solid's initial configuration. Exploiting the properties of proportionality, the dissipation inequality is fulfilled by the relations

$$\begin{aligned} (\phi^S)'_S &= -\frac{1}{M} \left[\rho_0^S \frac{\partial \psi^S}{\partial \phi^S} - \operatorname{div} \left(\rho_0^S \frac{\partial \psi^S}{\partial \operatorname{grad} \phi^S} \right) \right], \\ \mathbf{T}_E^L &= 2(\phi^S)^2 n^L \mu^{LR} \mathbf{D}_L \quad \text{and} \\ \hat{\mathbf{p}}_E^L &= -(1 - \phi^S)^2 \frac{(n^L)^2 \mu^{LR}}{K^S} \mathbf{w}_L. \end{aligned} \quad (9)$$

In this regard, the structure of the evolution equation for ϕ^S in (9)₁ is found under thermodynamical considerations. Therein, the mobility parameter M is introduced with a dual meaning, cf. Miehe et al. [36]. Physically, it governs the time-delay of fracture initiation and propagation and, furthermore, enables numerical stabilisation. Typically, the value for M is chosen very small. From (9)₁, it is clearly seen that only the energetic changes of the porous solid influence the evolution of ϕ^S . However, in the here considered coupled problem the related solid deformation can also be indirectly caused by the pore liquid's pressure. In (9)₂, the viscous extra stress \mathbf{T}_E^L of the liquid depends in addition to the effective dynamic viscosity μ^{LR} and the deformation velocity tensor \mathbf{D}_L also on the phase-field parameter ϕ^S . Therefore, the liquid extra stress \mathbf{T}_E^L

automatically vanishes in the intact porous domain but arises in the fractured zone. In (9)₃, the extra part of the direct liquid momentum production term $\hat{\mathbf{p}}_E^L$ depends in contrary fashion on ϕ^S such that $\hat{\mathbf{p}}_E^L$ disappears in the fully fractured zone but governs the pore-fluid flow in the intact porous domain. According to the fundamental papers of Kuhn and Müller [30] and Miehe et al. [36], the solid free energy is introduced as

$$\begin{aligned} \rho_0^S \psi^S(\boldsymbol{\varepsilon}_S, \phi^S, \text{grad } \phi^S) = & \left[(1 - \phi^S)^2 + \eta_r^S \right] \rho_0^S \psi^{S+}(\boldsymbol{\varepsilon}_S^+) + \\ & + \rho_0^S \psi^{S-}(\boldsymbol{\varepsilon}_S^-) + \\ & + G_c \Gamma^S(\phi^S, \text{grad } \phi^S). \end{aligned} \tag{10}$$

In particular, a combination of the tensile energy $\rho_0^S \psi^{S+}$, the compression energy $\rho_0^S \psi^{S-}$ and the fracture energy is chosen. The fracture energy includes the critical energy release rate G_c of brittle fracture. Physically, this parameter can be understood as a crack resistance property of the solid. From a microscopic perspective, G_c is linked to the energy required to break bonds between particles and, as a result, for the generation of an evolving fracture surface. Moreover, the fracture surface density function $\Gamma^S(\phi^S, \text{grad } \phi^S) = (\phi^S)^2 / 2\epsilon + \frac{1}{2} \epsilon \text{grad } \phi^S \cdot \text{grad } \phi^S$ is included in (10) in terms of a diffuse approach to fracture using the length-scale parameter ϵ . In particular, ϵ controls the width of the transition zone such that a decreasing ϵ sharpens the fracture towards a discrete (sharp) crack for $\epsilon \rightarrow 0$, as exemplarily shown for a one-dimensional case in Fig. 1.

According to Miehe et al. [36], a spectral decomposition of the symmetric strain tensor $\boldsymbol{\varepsilon}_S$ in terms of eigenvalues and eigenvectors allows for a split of $\boldsymbol{\varepsilon}_S = \boldsymbol{\varepsilon}_S^+ + \boldsymbol{\varepsilon}_S^-$ into positive and negative parts, cf. Ehlers and Luo [17].

Therefore, the solid free energy parts in (10) can be expressed as

$$\begin{aligned} \rho_0^S \psi^{S+}(\boldsymbol{\varepsilon}_S^+) = & \mu^S (\boldsymbol{\varepsilon}_S^+ \cdot \boldsymbol{\varepsilon}_S^+) + \\ & + \frac{1}{2} \lambda^S \left\{ \frac{1}{2} (\text{tr } \boldsymbol{\varepsilon}_S + |\text{tr } \boldsymbol{\varepsilon}_S|) \right\}^2, \\ \rho_0^S \psi^{S-}(\boldsymbol{\varepsilon}_S^-) = & \mu^S (\boldsymbol{\varepsilon}_S^- \cdot \boldsymbol{\varepsilon}_S^-) + \\ & + \frac{1}{2} \lambda^S \left\{ \frac{1}{2} (\text{tr } \boldsymbol{\varepsilon}_S - |\text{tr } \boldsymbol{\varepsilon}_S|) \right\}^2. \end{aligned} \tag{11}$$

Furthermore, a residual stiffness η_r^S is added in (10) in the tensile part of the strain energy to maintain a small stiffness in the fully damaged state.

The thermodynamical restriction (8)₁ can be evaluated using (10) to obtain the linearised effective stress tensor

$$\begin{aligned} \boldsymbol{\sigma}_E^S = & \rho_0^S \frac{\partial \psi^S}{\partial \boldsymbol{\varepsilon}_S} \\ = & \left[(1 - \phi^S)^2 + \eta_r^S \right] \left[2\mu^S \boldsymbol{\varepsilon}_S^+ + \frac{1}{2} \lambda^S (\text{tr } \boldsymbol{\varepsilon}_S + |\text{tr } \boldsymbol{\varepsilon}_S|) \mathbf{I} \right] + \\ & + 2\mu^S \boldsymbol{\varepsilon}_S^- + \frac{1}{2} \lambda^S (\text{tr } \boldsymbol{\varepsilon}_S - |\text{tr } \boldsymbol{\varepsilon}_S|) \mathbf{I} \end{aligned} \tag{12}$$

of the solid skeleton. In accordance, the evaluation of (9)₁ with (10) yields the evolution equation of ϕ^S as

$$(\phi^S)'_S = \frac{1}{M} \left[2(1 - \phi^S) \rho_0^S \psi^{S+} - G_c \left(\frac{\phi^S}{\epsilon} - \epsilon \text{div grad } \phi^S \right) \right]. \tag{13}$$

In the numerical approach, the restriction $(\phi^S)'_S \geq 0$ is considered using a history variable $\mathcal{H} = \max_{t > t_0} (\rho_0^S \psi^{S+})$ to account for irreversible fracturing processes, cf. Miehe et al. [36]. Moreover, to prescribe pre-fractured areas in the numerical approach, (13) is exploited to obtain the initial value \mathcal{H}_0 of the history variable using the assumption of a fully developed crack with $(\phi^S)'_S = 0$, yielding $\mathcal{H}_0 = G_c \phi^S / [2\epsilon(1 - \phi^S)]$. Therein, \mathcal{H}_0 would tend

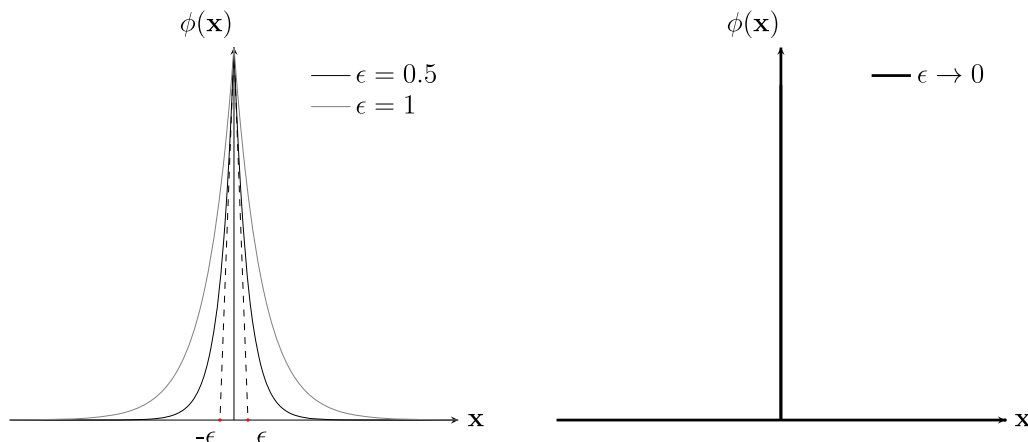


Fig. 1 Diffusive representation of a fracture using the phase-field approach (left) and a sharp fracture representation for the limit case $\epsilon \rightarrow 0$ (right)

towards infinity for $\phi^S = 1$. Therefore, ϕ^S is chosen slightly smaller than 1, such that $\phi^S \approx 1$ adjusts. In particular, the corresponding value can then be assigned, based on the phase-field material parameters of the considered problem, as an initial condition to describe a predefined notch within the domain. Finally, integrating (8)₂ and applying the Gaussian integral theorem leads to the boundary condition $G_c \epsilon \text{grad } \phi^S \cdot \mathbf{n} = 0$ for the phase-field variable, cf. Ehlers and Luo [17].

As described in Ehlers and Luo [17, 18], a monolithic solution of the strongly coupled set of governing equations for the biphasic TPM-phase-field model is used. In particular, the mass and momentum Eq. (2) and the evolution equation of the phase field (13) are closed by the admissible constitutive relations and result in the following weak formulations, cf. Ehlers and Luo [17]:

$$\begin{aligned}
 \mathcal{G}_p(\mathbf{y}) &= \int_B \{ \text{div} \mathbf{v}_S \delta p - n^L \mathbf{w}_L \cdot \text{grad } \delta p \} dv + \\
 &\quad + \int_S \underbrace{(n^L \mathbf{w}_L \cdot \mathbf{n})}_{=: \bar{v}} \delta p da = 0, \\
 \mathcal{G}_{\mathbf{u}_S}(\mathbf{y}) &= \int_B \left\{ \left(\rho^S (\mathbf{v}_S)'_S + \right. \right. \\
 &\quad \left. \left. + \rho^L [(\mathbf{v}_L)'_S + (\text{grad } \mathbf{v}_L) \mathbf{w}_L] \right) \cdot \delta \mathbf{u}_S + \right. \\
 &\quad \left. + (\boldsymbol{\sigma}_E^S + \mathbf{T}_E^L - p \mathbf{I}) \cdot \text{grad } \delta \mathbf{u}_S \right\} dv - \\
 &\quad - \int_S \underbrace{\left((\boldsymbol{\sigma}_E^S + \mathbf{T}_E^L) \mathbf{n} - p \mathbf{n} \right)}_{=: \bar{\mathbf{t}}} \cdot \delta \mathbf{u}_S da = 0, \\
 \mathcal{G}_{\mathbf{v}_L}(\mathbf{y}) &= \int_B \left\{ \left(\rho^{LR} [(\mathbf{v}_L)'_S + (\text{grad } \mathbf{v}_L) \mathbf{w}_L] - \right. \right. \\
 &\quad \left. \left. - \frac{1}{n^L} p \text{grad } n^L - \frac{1}{n^L} \hat{\mathbf{p}}_E^L \right) \cdot \delta \mathbf{v}_L + \right. \\
 &\quad \left. + \left(\frac{1}{n^L} \mathbf{T}_E^L - p \mathbf{I} \right) \cdot \text{grad } \delta \mathbf{v}_L \right\} dv - \\
 &\quad - \int_S \underbrace{\left(\frac{1}{n^L} \mathbf{T}_E^L \mathbf{n} - p \mathbf{n} \right)}_{=: \bar{\mathbf{t}}^{LR}} \cdot \delta \mathbf{v}_L da = 0, \\
 \mathcal{G}_{\phi^S}(\mathbf{y}) &= \int_B \left\{ \left[M(\phi^S)'_S - 2(1 - \phi^S) \mathcal{H} + \frac{G_c}{\epsilon} \phi^S \right] \delta \phi^S + \right. \\
 &\quad \left. + G_c \epsilon \text{grad } \phi^S \cdot \text{grad } \delta \phi^S \right\} dv - \\
 &\quad - \int_S G_c \epsilon \text{grad } \phi^S \cdot \mathbf{n} \delta \phi^S da = 0.
 \end{aligned} \tag{14}$$

These weak formulations are numerically implemented in the finite-element solver PANDAS (Porous media Adaptive Nonlinear finite-element solver based on Differential

Algebraic Systems, <http://www.get-pandas.com>). Thereby, the spatial domain is discretised with Taylor-Hood elements, cf. Fortin and Brezzi [20], and an implicit finite-difference scheme is used for the discretisation in time. By default, quadratic shape functions for \mathbf{u}_S and \mathbf{v}_L and linear shape functions for p and ϕ^S are chosen. Note that the solid displacement-velocity relation

$$\mathcal{G}_{\mathbf{v}_S}(\mathbf{y}) = \int_B [(\mathbf{u}_S)'_S - \mathbf{v}_S] \cdot \delta \mathbf{v}_S dv = 0 \tag{15}$$

is used here to reduce the overall momentum balance from second order to first order in time. A fully coupled solution (monolithic) strategy for the strongly coupled problem was used since this procedure has proven to be accurate and robust.

3 Experimental setup und results

To study the behaviour of NHF under in situ loading conditions, a triaxial testing environment is used. Therein, we performed pressure-diffusion-controlled pure tensile fractures in cylindrical samples. In this study, the samples consist of dense and low permeable Anröchter sandstone (Bentheim formation). Preliminary tests to obtain material parameters were performed on the sandstone samples. In particular, a one-dimensional deformation (compression) test resulted a Young's modulus of $E = 30$ GPa. The Darcy permeability (hydraulic conductivity) $k^L = 2 \times 10^{-11}$ m/s was estimated via a Darcy permeability test. Moreover, the densities of the components were measured and, thereof, a porosity of $n^L = 0.17$ was determined. These values are used in the numerical simulations, combined with further material parameters given in Table 2.

In the main experiment, hydrostatic conditions and subsequent changes of mechanical and hydraulic loading conditions are investigated. In this regard, the experimental procedure is motivated by the pioneering work of French et al. [22] but fully implemented and investigated at the Porous Media Lab (PML) of the Institute of Applied Mechanics, University of Stuttgart. The experimental setup is shown in Fig. 2. The external loading is applied using two separated pumps (Teledyne Isco syringe pump 100DX, max. pressure of 689 bar, volume of 100 ml with flowrates of 0.01 $\mu\text{l}/\text{min}$ to 50 ml/min) which are individually connected to the triaxial cell, as shown in Fig. 2. In this regard, the pump A is responsible to adjust the mechanical confining pressure onto the outer surface of the coated sandstone cylinder. In particular, the specimen was covered by a shrinkage tube in order to isolate the pore and the confining pressure. The pump B applies the hydraulic pore pressure of the fluid (water) via a tube onto a part of the top

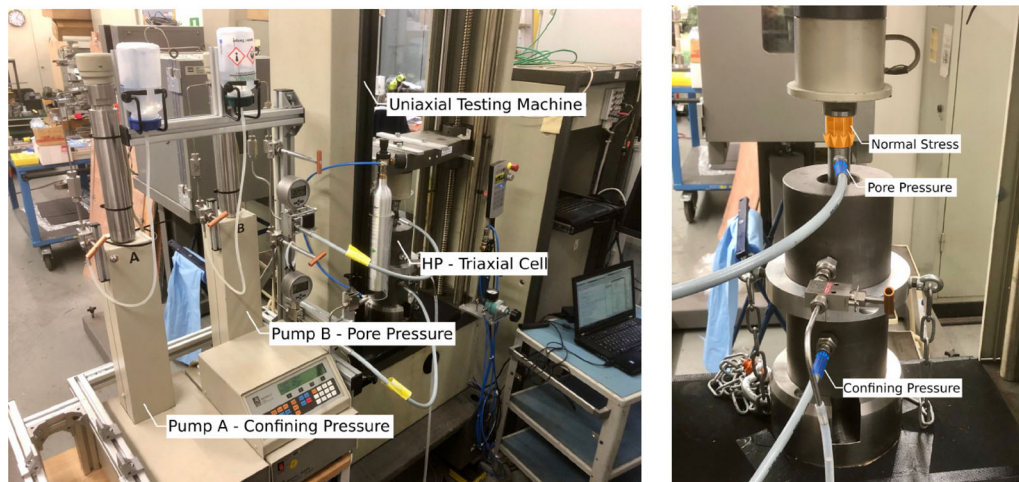
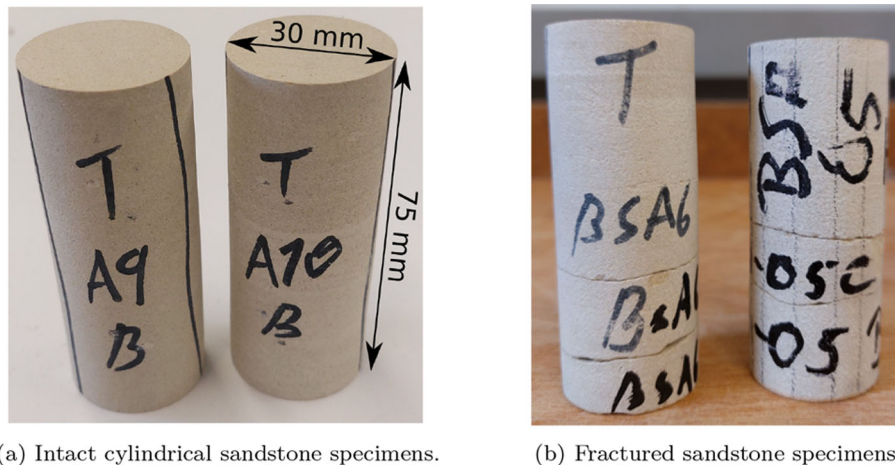


Fig. 2 Complete arrangement of the NHF experimental setup (left) and detail of the triaxial cell with connections (right)



(a) Intact cylindrical sandstone specimens.

(b) Fractured sandstone specimens.

Fig. 3 Cylindrical sandstone samples: **a** before the experiment and **b** after the experiment

surface of the cylinder. The change of the in situ stress state is achieved by a specific loading and unloading of the mechanical normal pressure in vertical direction, see Fig. 2b. The cylindrical specimen has a height of 75 mm and a diameter (width) of 30 mm, as shown in Fig. 3a.

As already mentioned, tensile stresses are required to obtain NHF in the sandstone matrix. The occurrence of tensile stresses in the solid material is an indirect result of unloading from a previous steady state (in situ) condition. In this regard, the experimental schema is designed as follows to capture these two properties. The cylindrical specimen is firstly placed into the triaxial test cell and is fully saturated therein. Then, this step is followed by applying the mechanical confining pressure and the hydraulic pore pressure to mimic the in situ loading state. Once the specimen achieves a steady flow state, the valve at the outlet, which confines the pore-fluid flow, is opened.

Thus, the pore pressure at the outlet becomes atmospheric pressure. Simultaneously, the pore pressure at the inlet is controlled to be close to atmospheric pressure accordingly. With sub-seconds of delay, subsequently, the normal stress is eliminated. Thus, the specimen could be deformed by the remaining pore pressure in it. A detailed description of the loading protocol for BSA01(2), the first experiment where a crack occurred, is given in Chapter 4 for the numerical simulation of this case. For all experiments, the confining pressure σ_c is chosen 2 MPa higher than the vertical (normal) pressure σ_n , where the latter is 1 MPa higher than the pore pressure p , cf. Fig. 5. Note that in the TPM-phase-field model the confining stress σ_c as well as the vertical (normal) stress σ_n are considered in terms of the classical mechanical sign convention, i. e. tensile stresses are positive, while the pore pressure p is, as common, positive for compressive stresses.

Table 1 Collection of the performed experiments on sandstone samples

Summary of experimental results			
Label	σ_c (MPa)	Pieces	Description of crack location
BSA01(1)	50	1	No crack
BSA01(2)	65	2	1/3 from bottom
BSA02	70	Broken	Broken
BSA03(1)	64	1	No crack
BSA03(2)(p)	50	2	2/3 from bottom
BSA04(1)	64	1	No crack
BSA04(2)(p)	50	2	2/3 from bottom
BSA05(p)	50	3	Two cracks close to the bottom (15 mm distance between the cracks)
BSA06(p)	50	3	Two cracks close to the bottom (18 mm distance between the cracks)
BSA07(p)	50	4	Three cracks at the middle
BSA08(p)	45	1	No crack

As a result of the experiments it is found that, along with the removing vertical pressure, the specimen is fractured horizontally, as shown in Fig. 3b for the samples BSA05 and BSA06. For an overview, Table 1 collects the results for the performed experiments on eight sandstone samples. In Table 1, the confining pressure σ_c has been set differently in the experiments. Furthermore, the pieces of the sample after the experiment and a rough description of the crack location(s) is given. It is obvious that the obtained results are quite different, which may come from a variety of influences. In this regard, main issues are supposed to be the lack of prior knowledge of local (microscopic) weak points or inhomogeneities, while the exact manual execution of the loading protocol is extremely challenging. Moreover, after several attempts, the top and bottom surfaces of samples were polished (p) to achieve a better fit to the testing machine. This prevented a rupture of the used shrinkage tube caused by high confining pressure. As a result, this leads to different crack patterns. Furthermore, the number of cracks varies, sometimes the sample is completely ruined, cf. BSA02, or remains intact, cf. BSA08. Therefore, the numerical recalculation in the following chapter is used to further study and discuss these experimental outcomes for different scenarios.

4 Numerical simulation and comparison with experiments

In this chapter, a numerical model is developed in accordance to the experiments described in Chapter 3 to simulate the natural hydraulic fracturing behaviour of sandstone. The chosen material parameters for the solid and liquid components of the saturated sandstone samples are either obtained by preliminary experiments on the sandstone samples, cf. Chapter 3, or taken from the book of Morrow et al. [38]. For example, the Lamé constants are found by a combination of the experimentally obtained Young's modulus of $E = 30$ GPa with a chosen Poisson ratio of $\nu = 0.26$, based on Morrow et al. [38]. In addition, the phase-field parameters are meaningfully chosen for the simulations of the fracturing experiments with pure tensile crack(s). The length-scale parameter ϵ is chosen small to ensure a clear crack pattern. Here, no value for the crack resistance G_c is given, since this parameter is studied in Sect. 4.2.1. A collection of all used material parameters is given in Table 2.

To reduce the computational effort, the three-dimensional cylindrical samples under the symmetrical triaxial stress state are simulated using an axisymmetric two-dimensional model, as is common practise cf., e. g., the book of Helwany [26]. In this case, the rectangular geometry with height $h = 75$ mm and width $w = 15$ mm is discretised with 2440 quadrilateral Taylor-Hood elements. In

Table 2 Collection of material parameters for the numerical simulations

Collection of material parameters			
	Value	Unit	Description
μ^S	11.904	[GPa]	Lamé constant of φ^S (experimentally based)
λ^S	12.896	[GPa]	Lamé constant of φ^S (experimentally based)
ρ^{SR}	3 000	[kg/m ³]	Real density of φ^S (experimentally based)
ρ^{LR}	1 000	[kg/m ³]	Real density of φ^L (experimentally based)
μ^{LR}	0.001	[Pa s]	Dynamic viscosity of φ^L (water)
n_{0S}^S	0.83	[-]	Initial solidity of φ^S (experimentally based)
K^S	2.0×10^{-18}	[m ²]	Intrinsic permeability (experimentally based)
M	0.001	[Pa s]	Mobility parameter
ϵ	5.0×10^{-6}	[m]	Length-scale parameter
η_r^S	1.0×10^{-3}	[-]	Residual artificial stiffness of φ^S

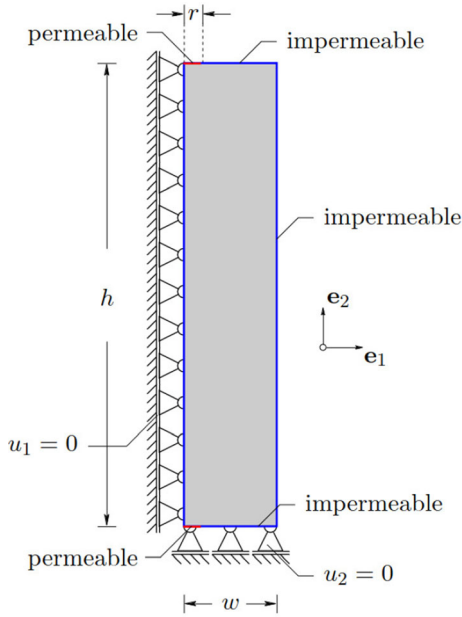
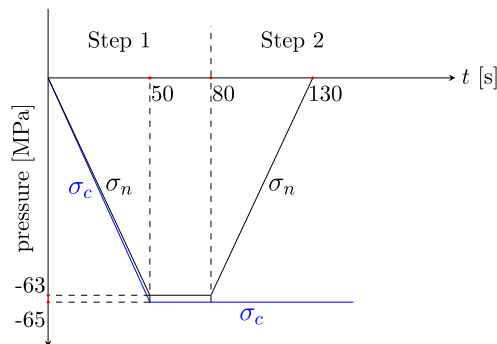


Fig. 4 Geometry and boundary conditions for the simulation of the triaxial sandstone experiment

terms of the Dirichlet-type mechanical boundary conditions, the vertical symmetry line of the specimen is fixed in the horizontal direction and the bottom of the sample is fixed in the vertical direction, as shown in Fig. 4. Two small tubes with an inner diameter of 3.5 mm (radius $r = 1.75$ mm) in the center of the top and bottom surfaces allow the application of the hydraulic boundary conditions for the fluid. In particular, a Dirichlet-type pressure boundary condition is assigned to the tube areas and results in free-flow boundary condition, i. e. in a permeable surface. All of the remaining edges are considered as impermeable (no-flow boundary condition). The basic setup of the geometry as well as the mechanical support and the hydraulic permeability conditions of the outer boundaries are identical for all experiments.



(a) Vertical and confining pressure over time.

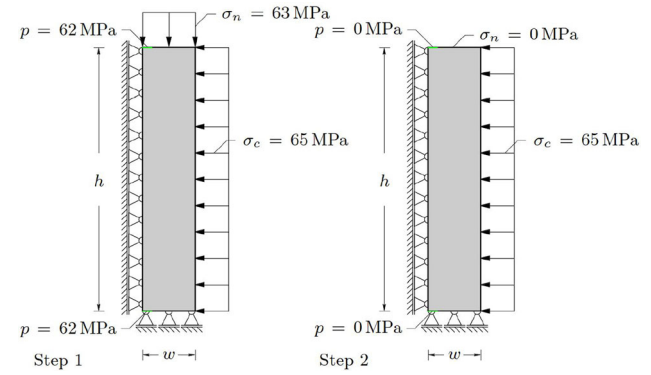
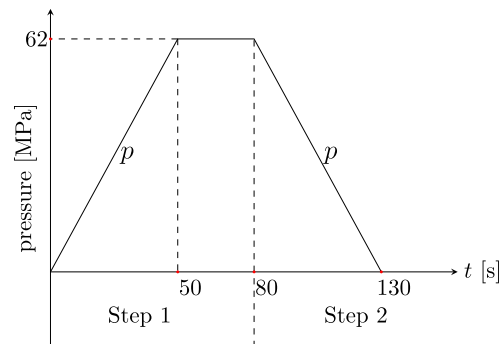


Fig. 6 Geometry and loading of the triaxial sandstone experiment: loading in Step 1 (left) and unloading in Step 2 (right)

The loading history is chosen here according to the first successful experiment BSA01(2), cf. Table 1. Basically, the loading procedure is divided into two steps, shown in Fig. 5 for the vertical (normal) stress σ_n , the confining pressure σ_c and the pore pressure p . The application of the loading to the sample is shown in Fig. 6. In the first step (loading), the vertical and confining pressures are increased within 50 s to 63 MPa and 65 MPa, respectively. Particularly, this leads for the Neumann boundary conditions in (14)₂ to $\bar{t}_1 = \sigma_n = -63$ MPa and $\bar{t}_2 = \sigma_c = -65$ MPa after 50 s. Moreover, pore pressure boundary conditions are applied via the tube from the top and bottom, again loaded within 50 s to 62 MPa. The loading state is held for further 30 s, to obtain a homogeneous pore pressure distribution within the entire specimen. In the second step (unloading), the vertical loading and applied pore pressure drop to zero within 50 s, while the confining pressure remains. In this regard, the same time span as for the loading stage is used. Obviously, this is different in comparison to the conducted experiments, where the load is suddenly removed. However, a longer unloading step allows a better control of the fracturing process and leads to a numerically stable computation without convergence problems. In general, the



(b) Pore pressure over time.

Fig. 5 Loading protocol for the mechanical parts: vertical (normal) stress σ_n and confining pressure σ_c . The hydraulic part is represented by the pore pressure p

basic effect of NHF is not affected by this time scaling, in particular under the circumstance that the time of crack occurrence is not considered in this study. Note in passing that the assumption of materially incompressibility for the liquid (water) constituent is only valid for moderate pressures. However, relatively high pressures of up to 62 MPa are applied in the experiments and may change the water volume up to 2.5–3.0 %. Nevertheless, for the aspects examined in this study we consider it sufficient to neglect the compressibility in the present modelling approach.

4.1 Results for the biphasic TPM model without fracturing

Before modelling the fracturing process, the basic coupled material behaviour during the triaxial experiment, i. e. the arising stress distribution within the sandstone sample, is derived in this subsection. Therefore, the basic biphasic model of Sect. 2.1 without an embedded phase-field approach to fracture is applied to the loading protocol described in Fig. 5. In particular, the boundary conditions, cf. Fig. 6, include the external loading and the applied pore pressure according to the loading procedure, cf. Fig. 5. During the loading process, a typical consolidation behaviour is observed which reaches equilibrium stress at the end of the first loading step, cf. Fig. 7. At this point, the specimen has a homogeneously distributed pore pressure of $p = 62$ MPa and a total vertical (compression) stress $\sigma_{22} = -63$ MPa. Based on the principle of effective stresses

$$\boldsymbol{\sigma} = \boldsymbol{\sigma}_E^S - p \mathbf{I}, \quad (16)$$

this equilibrium stress state results in an effective (compression) stress of $\sigma_{E22}^S = -1$ MPa within the solid skeleton. This equilibrium stress state can be interpreted as the initial equilibrium state of geomaterials under in situ conditions. After the stresses have reached equilibrium, the total stress σ_{22} and the pore pressure p start to drop to

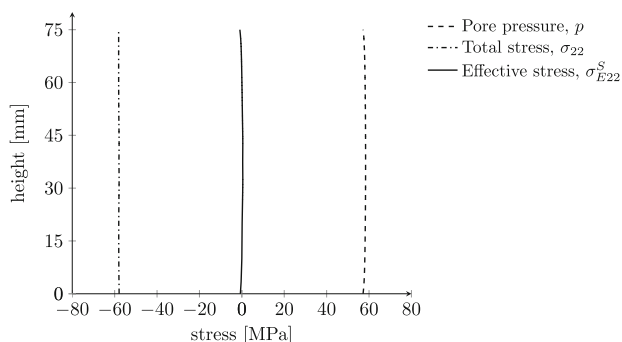


Fig. 7 Stress partition under external loading in the equilibrium state of Step 1

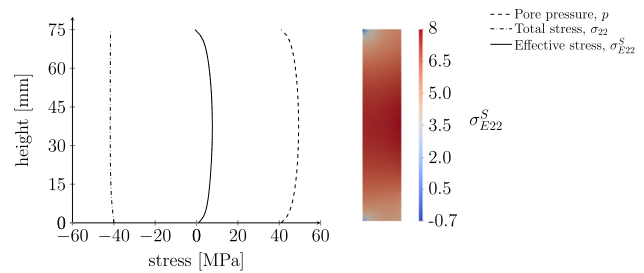


Fig. 8 Stress partition during the Step 2 (unloading) with the measured Darcy permeability of $k^L = 2 \times 10^{-11}$ m/s

mimic changes in the loading conditions at deep subsurface foundations.

The decrease of the vertical load and the zeroing of the fluid pressure leads to a pore pressure diffusion and tensile stresses within the specimen, as shown in Fig. 8. In particular, this is caused by the permeability which restrains the fluid from going out through the open tube on the top and bottom surfaces. Therefore, the pore pressure in the middle takes more time to decrease than that in the area near the open tube on the top and bottom surfaces, thus creating a pore pressure gradient and diffusive behaviour over time. As the total vertical pressure is reduced and the pore pressure is maintained, the effective stress within the solid skeleton has to increase to balance the external total stress, cf. (16). This process essentially depends on the permeability, as can be seen in Fig. 9 for a four-times higher permeability value. In this case, the effective stresses within the solid only changes marginally since the fluid is able to flow out easily.

From the stress state analysis of the recalculated triaxial experiment, it can be concluded that during the unloading Step 2, the sandstone sample develops tensile effective stresses under the considered loading protocol. This provides the possibility of fracture evolution within the solid skeleton if the tensile stresses exceed the strength of the material. Therefore, the permeability of a geological material plays an important role for the occurrence of NHF.

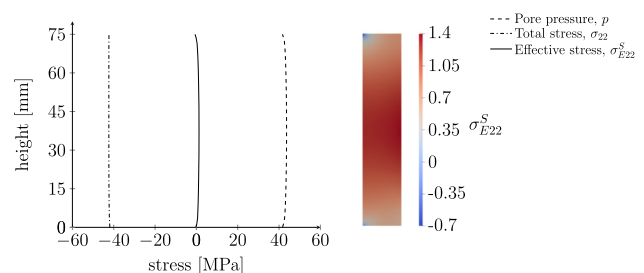


Fig. 9 Stress state during the Step 2 (unloading) with a four-times higher Darcy permeability of $k^L = 8 \times 10^{-11}$ m/s

4.2 Results for the biphasic TPM model with embedded phase-field approach to fracture

In this subsection, the fracturing behaviour is studied with a specific focus on the influence of the phase-field parameter G_c and the permeability.

4.2.1 Effect of the critical energy release rate G_c on the fracture evolution

As indicated in (10), the critical energy release rate G_c represents the resistance of the material to fracturing. Therefore, G_c is one of the key parameters responsible for the fracturing behaviour. Since there are no comparable studies of NHF of sandstone within the framework of the TPM-phase-field method, an estimated value of G_c is firstly chosen from the related literature. Based on that, a sensitivity study is performed afterwards to justify the range of the critical value of G_c that permits a fracture occurrence.

In the literature, several values for G_c of geomaterials in phase-field approaches can be found. For example, Prajapati et al. [40] reported a value of $G_c = 57$ N/mm in a study related to the anisotropic fracture propagation of an artificial sandstone consisting only on quartz grains. Therein, a good agreement on the anisotropic fracture behaviour was obtained by varying G_c with the crystallographic orientation of each quartz grain. However, it was also mentioned that the adopted material parameter may not be applicable to real geological systems. In another study, Ip and Borja [27] reported a value of $G_c = 42$ N/mm for Bentheim sandstone in terms of modelling the formation of compaction bands under compression. In this model, G_c shares the same physical meaning of the energy release rate as in fracture modelling, but is used only for the compressive stress state. In conclusion, it can be stated that a precise quantification of G_c on the NHF is still missing.

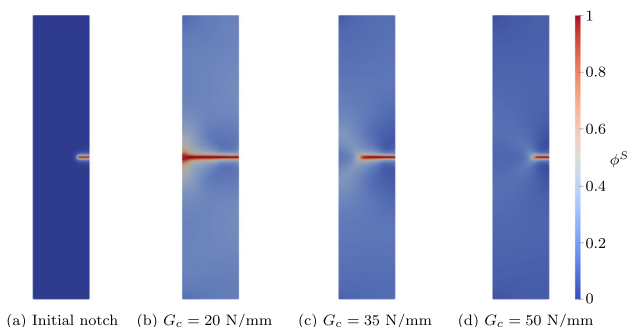


Fig. 10 Influence of lower values for G_c on the fracturing behaviour at $t = 112$ s

Based on the above mentioned two studies, three different values for G_c are investigated here: 20 N/mm for a weak crack, 35 N/mm for a normal crack and 50 N/mm for a strong crack resistance. The other parameters remain constant for all simulations as given in Table 2. Furthermore, an initial crack (notch) of 3 mm length is predetermined at the middle of the sample via the assignment of a pseudo-elastic energy \mathcal{H}_0 corresponding to a phase field $\phi \approx 1$, cf. Borden et al. [8] and Ehlers and Luo [18].

Figure 10 shows the sandstone fracture evolution under the three different values of G_c at $t = 112$ s, i. e. in the middle of the unloading history. For $G_c = 20$ N/mm, a through-going crack is already developed. In contrast, the crack is just about to grow for $G_c = 50$ N/mm. It can be recognised, that the fracture development for the $G_c = 35$ N/mm case fits best to the experimental results. As expected, the results show that the crack propagation is retarded with increasing resistances G_c . Due to the assumption of homogeneous material with constant

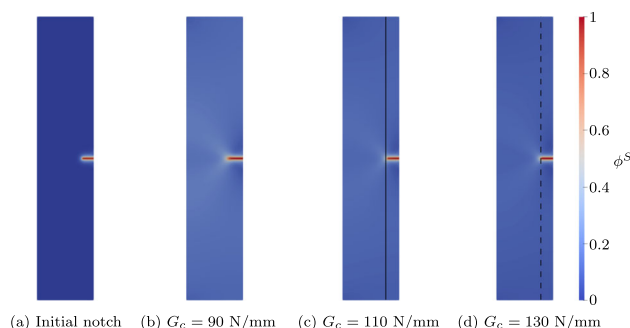


Fig. 11 Influence of higher values for G_c on the fracturing behaviour

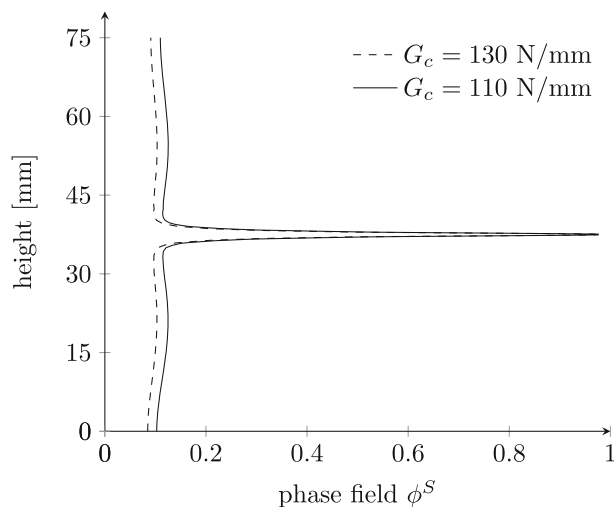


Fig. 12 Degree of damage (phase-field evolution) over the height of the cylinder at the level of the initial crack tip (cf. the solid and dotted black lines marked in Fig. 11) for higher values of G_c preventing fracture propagation

material parameters, the propagating cracks remain purely horizontal, as the initial notch has been assumed horizontal. In principle, it is also possible to consider crack branching or non-horizontal fractures within the TPM-phase-field approach if material imperfections or heterogeneities are taken into account, cf. Wagner et al. [46]. The inclusion of spatially varying material parameters may help to reproduce the experimental results, cf. Fig. 3b. However, this was not intended here due to the lack of microstructural knowledge of the sandstone samples.

In engineering practise, it is necessary to know the critical value of G_c to prevent a fracture evolution. In this regard, Fig. 11 shows the phase-field development, under higher G_c values at the end of the unloading process. In this study, it can be seen that the sandstone can not develop any fracture, but is only damaged, when $G_c > 110$ N/mm. According to the solid and dotted black lines, marked in Fig. 11 (c) and (d), the degree of damage over the height at the level of the initial crack tip is shown in Fig. 12 using the phase field.

4.2.2 Effect of the permeability on the fracture evolution

As discussed in Sect. 4.1, the permeability affects the pore pressure response during the unloading stage. In particular, a smaller permeability causes a more pronounced (steeper) pore pressure profile and results therefore in higher effective tensile stresses in the solid to balance the decreasing external load, cf. Fig. 8. These tensile stresses initiate fracture within the specimen.

Figure 13 and Fig. 14 show the fracture behaviour of the specimen at $G_c = 35$ N/mm over time for two different permeabilities, namely the original measured one of $k^L = 2 \times 10^{-11}$ m/s and a four-times higher one of $k^L = 8 \times 10^{-11}$ m/s. As expected from the basic coupled multiphase material behaviour described in Sect. 4.1, the specimen with the lower (original) permeability shows an evident evolution of fracture, cf. Fig. 13, while there is no

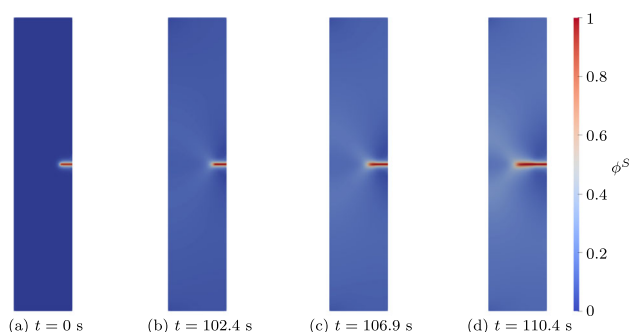


Fig. 13 Fracturing behaviour for a Darcy permeability of $k^L = 2 \times 10^{-11}$ m/s

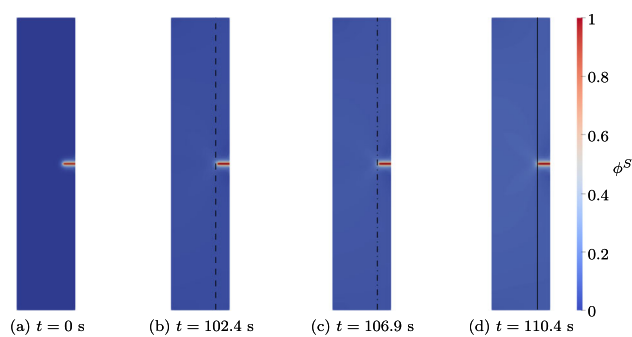


Fig. 14 Fracturing behaviour using a four-times higher Darcy permeability of $k^L = 8 \times 10^{-11}$ m/s

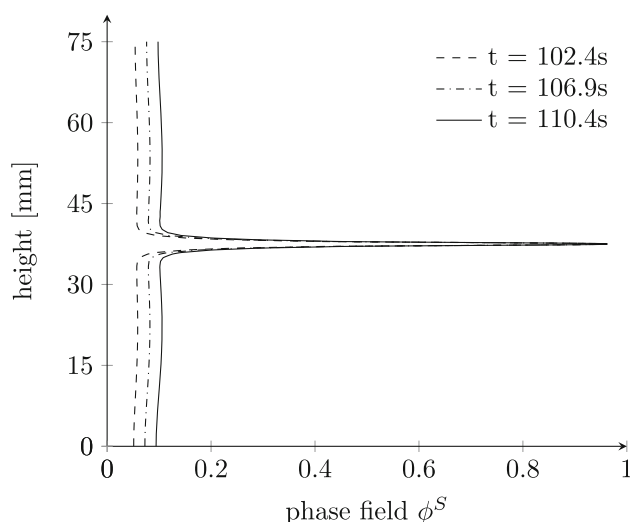


Fig. 15 Degree of damage (phase-field evolution) for $k^L = 8 \times 10^{-11}$ m/s at different times in front of the crack tip over the height (the line positions are shown in Fig. 14)

fracture occurrence (only damage effect) in the specimen with the higher permeability, cf. Fig. 14.

Correspondingly, the degree of damage evaluated by the phase field is presented in Fig. 15 for the higher permeability. The corresponding stress distribution for the two different permeabilities is given along the specimen's symmetry line in Fig. 16 at two specific time steps $t = 102.4$ s and $t = 110.4$ s for a more detailed analysis. It can be seen that after unloading at $t = 102.4$ s, the specimen with the lower (original) permeability has developed vertical effective tensile stresses in the solid skeleton all over its height, cf. Fig. 16a. In contrast, the specimen with the higher permeability still retain compression stresses at the top surfaces, cf. Fig. 16b.

With ongoing unloading, a significant increase in the tensile stresses is observed at $t = 110.4$ s in the middle of the lower (original) permeable specimen, as shown in Fig. 16c. This effect is obtained since at this point the sandstone has already fractured to a large extent, the

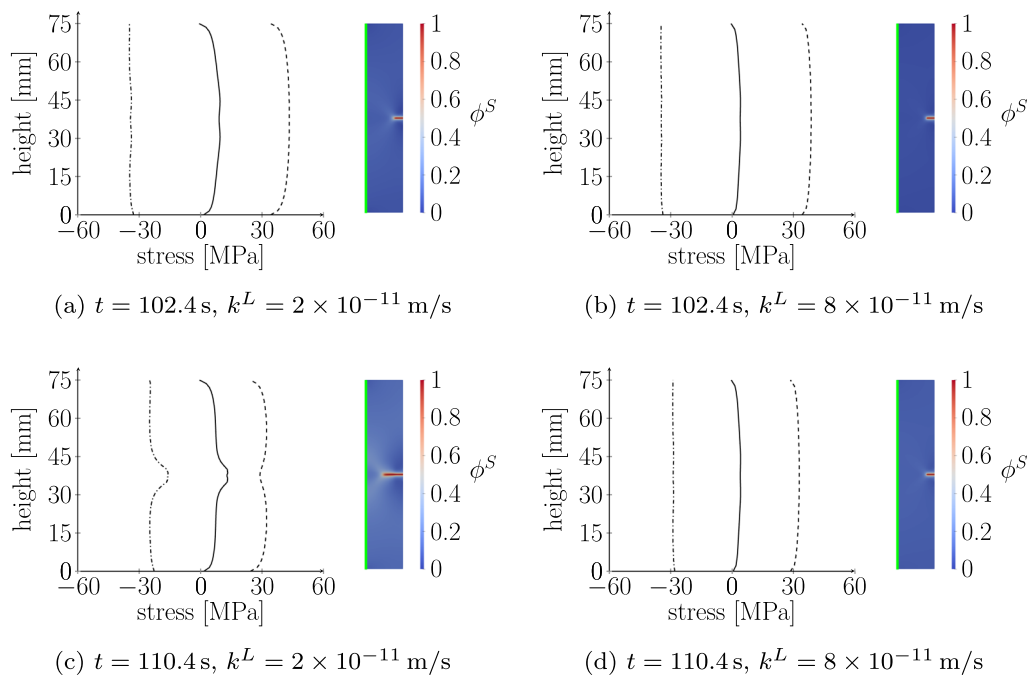


Fig. 16 Stress distribution and fracture evolution for two different times and permeabilities. The dashed dotted line indicates the total stress, the solid line the effective stress and the dashed line the pore pressure, given over the height along the green (symmetry) line

middle intact section decreases due to the propagation of the fracture and the remaining section has to carry all the external loads. Therefore, the tensile stresses increase within the remaining intact section. In other words, once the material starts to fracture, it will fracture at an increasing rate due to the increased stresses in the decreasing intact area.

For the specimen with higher permeability it is observed in Fig. 16d that during unloading at $t = 110.4$ s, the effective tensile stresses in the solid skeleton are very small and do not lead to a fracturing of the specimen, only to some damage effects. This behaviour can be explained by the fact that the fluid can flow out faster due to the larger permeability and, as a consequence, the pore pressure can also diffuse faster. Therefore, in accordance to (16), only a very small tensile stress is generated in this case.

As a result of this study on the influence of the permeability, an interesting property of NHF is revealed. It is found that the occurrence of NHF does not only depend on the external loads but also on the prevailing permeability of the material. Furthermore, it could be shown that NHF evolution is accompanied by a continuous decrease in the pore pressure. This is in contrast to IHF, where the pore pressure is typically increased to maintain a fracture evolution.

4.2.3 Study of fracture profiles and comparison with the experiments

Based on the symmetric setup of the studied experiment, the highest effective tensile stresses in the solid skeleton arise in the middle of the specimen. Therefore, we first expected a single complete fracture arising in the middle of the sample from the conducted experiments. This case was found, however, several samples show additional and non complete cracks at the upper and/or lower parts of the specimen, cf. Table 1 and Fig. 3b. Therefore, the modelling of additional incomplete cracks occurring at the upper and/or lower parts of the specimen is investigated in this subsection. Physically, incomplete fractures can develop since tensile stresses in the solid skeleton are

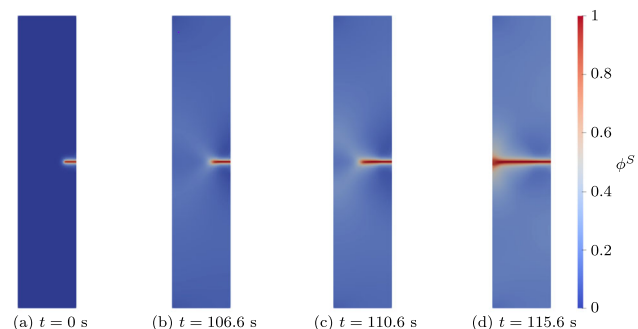


Fig. 17 Case (i): Evolution of a single complete crack from a central notch

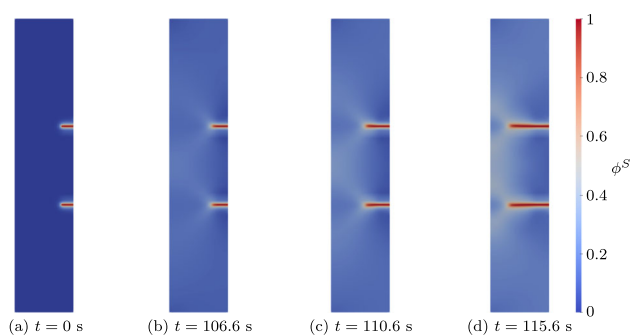


Fig. 18 Case (ii): Evolution of two incomplete symmetric cracks

present over the entire height of the sample but decreasing towards the top and bottom.

In this regard, different locations of pre-defined notches are investigated using for all simulations the basic material parameters from Table 2 and the estimated parameter $G_c = 35$ N/mm. The specification of notches naturally governs the resulting crack pattern and must therefore be understood as knowing the weak point(s) of the sample and thus the starting location of the crack(s) in advance. However, knowing the crack locations from the experiments, a simulation of an individual experimental case can be investigated to reconstruct and evaluate the fracturing process. In particular, three different cases are studied.

Case (i) considers a central complete crack occurring under perfect experimental (symmetrical application of the sample and the boundary conditions) and (homogeneous) material conditions. As shown in Fig. 17, the fracture evolves towards the line of symmetry with increasing speed as the external vertical load decreases. This fracture evolution corresponds to the experimental result of BSA01(2), BSA03(2) and BSA04(2), as summarised in Table 1. These samples showed a single complete crack, which, however, did not appear exactly in the middle.

Case (ii) assumes that the initial fractures are located at other places. Then, the evolution of two fractures located at the upper and lower part of the specimen is obtained as shown in Fig. 18. The two cracks are symmetrical with respect to the vertical midline of the specimen and evolve

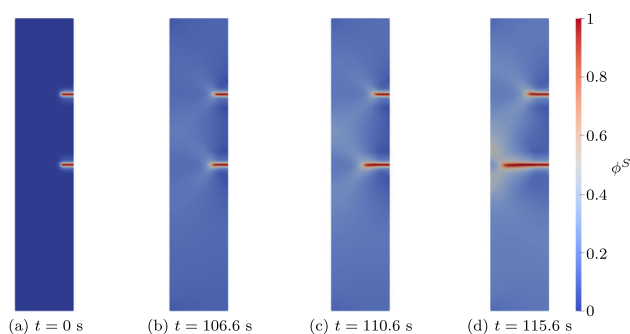


Fig. 19 Case (iii): Evolution of two incomplete asymmetric cracks

at the same velocity due to the identical effective tensile stresses in the solid skeleton. This fracturing behaviour was not observed in the experiments, cf. Table 1. This is due to the fact that a crack is most likely to appear at the point of maximum tensile stress. To obtain case (ii) in an experiment, there would have to be two symmetrical local weak points such that this crack pattern would occur.

Therefore, case (iii) studies the more realistic development of two asymmetric fractures which also occurred in the experiments at the samples BSA05 and BSA06, cf. Table 1 and Fig. 3b. In particular, the simulation results in one crack in the middle of the specimen and the other (asymmetric) one halfway to the drained boundary, cf. Fig. 19. Since the effective tensile stress in the solid, shown in Fig. 20, is larger in the middle than at the other part of the specimen, the fracture in the middle advances faster than the one in the upper part. Note that the effective tensile stress is evaluated along the specimen's symmetry line, marked as a green line in Fig. 20.

Moreover, a comparison of a single central full crack, case (i), with two asymmetric cracks, case (iii), is shown in Fig. 21. It is recognised that in case (i), the specimen is already broken completely while the specimen with two asymmetric fractures still preserves an intact part in the centre. This is due to the fact that in case (iii) a part of the strain energy is consumed by the fracture in the upper part of the specimen. Thus the central crack still remains incomplete in that case.

5 Conclusion

In this work, the evolution of natural hydraulic fractures (NHF) is studied using a combined experimental and simulation approach. In particular, we applied the modelling and simulation framework of the theory of porous media (TPM) with an embedded phase-field approach to fracture to experiments on sandstone (rock) cylinders under laboratory-created *in situ* conditions. Within this methodological framework, the processes during NHF initiation and evolution could be discussed and evaluated. As a result, the occurrence of NHF under arising effective tensile stresses in a low permeable dense sandstone caused by a drop of external load was justified.

In this regard, the hydraulic conductivity k^L and the critical energy release rate G_c have been identified to play a key role in the process of NHF. It was found that a lower permeability and/or critical energy release rate promotes the development of NHF. Thus, the study presented in this work provides meaningful insights for the engineering practise. For example, excessive fracture evolution within geomaterials may be avoided by either increasing the

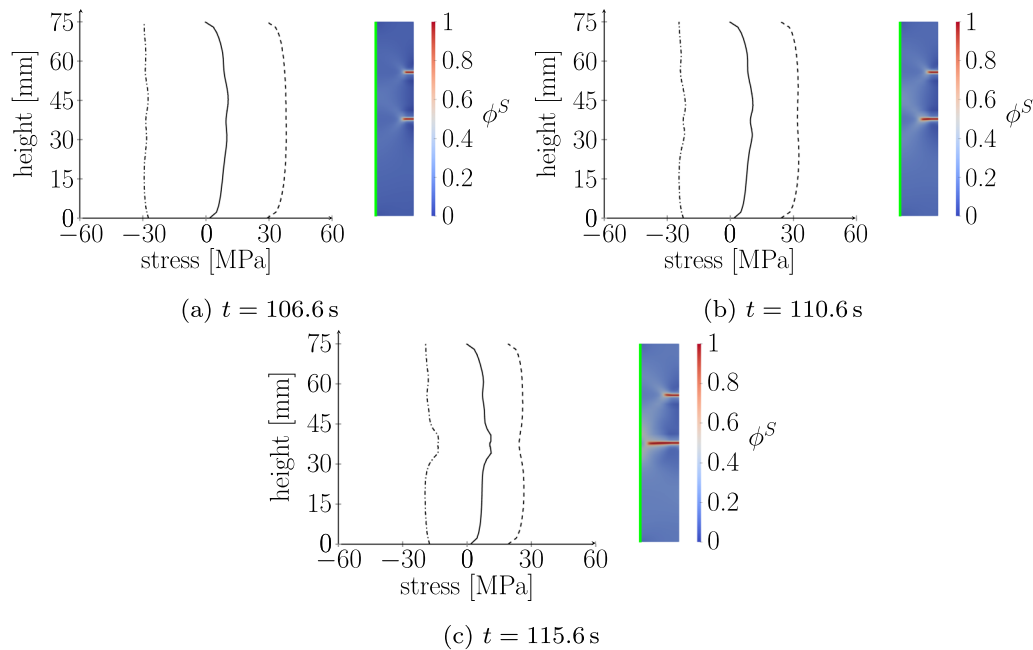


Fig. 20 Stress distribution over the height for case (iii) with two asymmetric cracks. The dashed dotted line indicates the total stress, the solid line the effective stress and the dashed line the pore pressure, given over the height along the green (symmetry) line

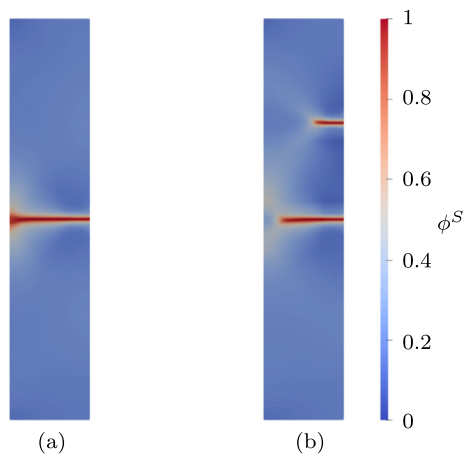


Fig. 21 Comparison between case (i) with a single central crack **(a)** and case (iii) with two asymmetric cracks **(b)** at $t = 115.6$ s

permeability or the critical energy release rate of the ground. In this study we have considered these effects independently. However, it should be noted that there may be a competing effect between permeability and critical energy release rate. In particular, an increasing permeability would correlate to a decreasing critical energy release rate, meaning that a simultaneous decrease or increase in permeability and critical energy release rate is not feasible. This is due to the fact that for certain materials the porosity and the critical energy release rate are dependent on each other, as was shown by Yang et al. [47] for ceramics with controlled (homogeneous) porosity. If, furthermore, the porous material shows a porosity-

permeability relationship, e. g. for a specific (ideal) porous material, as was used for the benchmark example in Wagner et al. [45], a competing effect between permeability and crack resistance occurs. However, for natural (heterogeneous) dense rock materials, the competing effect does not necessarily have to appear and is not addressed in this contribution. The interested reader is rather referred to the work of Ip & Borja [28], where a relationship between porosity and critical energy release rate is included and applied to model the permeability evolution in a compaction band of a heterogeneous porous material using a phase-field approach. In conclusion, the presented modelling approach allows for a prediction of the expected effects of a planned construction project for which the boundary conditions are known. In this regard, a critical range of $G_c > 110$ N/mm was found in the investigated experiments on sandstone cylinders to prevent fracturing. These findings can be of great interest when transferred to realistic geotechnical applications.

To the authors' knowledge, this work provides the first successful attempt to apply the TPM-phase-field method to describe NHF. It can finally be stated that the proposed model can serve as a powerful tool for engineering practise to study interventions in a natural (in situ) state.

Author Contributions WE, AW and HS conceptualised the project; JW, AS, DL, HS, AW and WE developed the methodological content of work; JW performed the numerical simulations; DL conducted the experiments; JW, AS, DL, HS, AW and WE analysed the results; Funding acquisition and supervision were done by GX, VAS, HS,

AW and WE; Resources were done by WE and HS; JW wrote the original draft of the manuscript; Review and editing of the manuscript were done by all authors. All authors have read and agreed to the published version of the manuscript.

Funding Open Access funding enabled and organized by Projekt DEAL. The work is funded by the Deutsche Forschungsgemeinschaft (DFG, German Research Foundation)—Project Number 327154368—SFB 1313. Furthermore, financial support from the Italian Ministry of Education, University and Research (MUR), in the framework of PRIN2020 #20209F3A37 Project, is gratefully acknowledged.

Declarations

Conflict of interest The authors declare no Conflict of interest.

Open Access This article is licensed under a Creative Commons Attribution 4.0 International License, which permits use, sharing, adaptation, distribution and reproduction in any medium or format, as long as you give appropriate credit to the original author(s) and the source, provide a link to the Creative Commons licence, and indicate if changes were made. The images or other third party material in this article are included in the article's Creative Commons licence, unless indicated otherwise in a credit line to the material. If material is not included in the article's Creative Commons licence and your intended use is not permitted by statutory regulation or exceeds the permitted use, you will need to obtain permission directly from the copyright holder. To view a copy of this licence, visit <http://creativecommons.org/licenses/by/4.0/>.

References

- Adachi J, Siebrits E, Peirce A, Desroches J (2007) Computer simulation of hydraulic fractures. *Int J Rock Mech Min Sci* 44:739–757
- Ambati M, Gerasimov T, De Lorenzis L (2015) Phase-field modeling of ductile fracture. *Comput Mech* 55:1017–1040
- Ambati M, Gerasimov T, De Lorenzis L (2015) A review on phase-field models of brittle fracture and a new fast hybrid formulation. *Comput Mech* 55:383–405
- Berre I, Boon WM, Flemisch B, Fumagalli A, Gläser D, Keilegavlen E, Scotti A, Stefansson I, Tatomir A, Brenner K et al (2021) Verification benchmarks for single-phase flow in three-dimensional fractured porous media. *Adv Water Resour* 147:103759
- Berre I, Doster F, Keilegavlen E (2019) Flow in fractured porous media: a review of conceptual models and discretization approaches. *Transp Porous Media* 130:215–236
- Biot MA (1941) General theory of three-dimensional consolidation. *J Appl Phys* 12:155–164
- Borden MJ, Hughes TJ, Landis CM, Anvari A, Lee IJ (2016) A phase-field formulation for fracture in ductile materials: finite deformation balance law derivation, plastic degradation, and stress triaxiality effects. *Comput Methods Appl Mech Eng* 312:130–166
- Borden MJ, Verhoosel CV, Scott MA, Hughes TJ, Landis CM (2012) A phase-field description of dynamic brittle fracture. *Comput Methods Appl Mech Eng* 217:77–95
- Bowen RM (1980) Incompressible porous media models by use of the theory of mixtures. *Int J Eng Sci* 18:1129–1148
- Bowen RM (1982) Compressible porous media models by use of the theory of mixtures. *Int J Eng Sci* 20:697–735
- Chen B, Barboza BR, Sun Y, Bai J, Thomas HR, Dutko M, Cottrell M, Li C (2022) A review of hydraulic fracturing simulation. *Archiv Comput Methods Eng* 29:1–58
- Cordero JAR, Sanchez ECM, Roehl D, Pereira LC (2019) Hydro-mechanical modeling of hydraulic fracture propagation and its interactions with frictional natural fractures. *Comput Geotech* 111:290–300
- Coussy O (2004) *Poromechanics*. Wiley, Hoboken
- Davies RJ, Mathias SA, Moss J, Hustoft S, Newport L (2012) Hydraulic fractures: How far can they go? *Mar Pet Geol* 37:1–6
- De Boer R (2012) *Theory of porous media: highlights in historical development and current state*. Springer, Berlin
- Ehlers W (2002) Foundations of multiphase and porous materials. In: Ehlers W, Bluhm J (eds) *Porous media: theory, experiments and numerical applications*. Springer, Berlin, pp 3–86
- Ehlers W, Luo C (2017) A phase-field approach embedded in the Theory of Porous Media for the description of dynamic hydraulic fracturing. *Comput Methods Appl Mech Eng* 315:348–368
- Ehlers W, Luo C (2018) A phase-field approach embedded in the Theory of Porous Media for the description of dynamic hydraulic fracturing, Part II: the crack-opening indicator. *Comput Methods Appl Mech Eng* 341:429–442
- Ehlers W, Wagner A (2019) Modelling and simulation methods applied to coupled problems in porous-media mechanics. *Arch Appl Mech* 89:609–628
- Fortin M, Brezzi F (1991) *Mixed and hybrid finite element methods, vol 2*. Springer, New York
- Francfort GA, Marigo JJ (1998) Revisiting brittle fracture as an energy minimization problem. *J Mech Phys Solids* 46:1319–1342
- French M, Boutt D, Goodwin L (2012) Sample dilation and fracture in response to high pore fluid pressure and strain rate in quartz-rich sandstone and siltstone. *J Geophys Res Solid Earth* 117:B03215
- Gale J, Elliott S, Li JZ, Laubach S (2019) Natural fracture characterization in the Wolfcamp formation at the hydraulic fracture test site (HFTS), Midland Basin, Texas. In: *SPE/AAPG/SEG Unconventional Resources Technology Conference*. OnePetro
- Griffith AA (1921) The phenomena of rupture and flow in solids. *Philosophical transactions of the Royal Society of London. Series A, containing papers of a mathematical or physical character* 221:163–198
- Heider Y, Markert B (2017) A phase-field modeling approach of hydraulic fracture in saturated porous media. *Mech Res Commun* 80:38–46
- Helwany S (2007) *Applied soil mechanics with ABAQUS applications*. Wiley, Hoboken
- Ip SC, Borja RI (2022) A phase-field approach for compaction band formation due to grain crushing. *Int J Numer Anal Meth Geomech* 46:2965–2987
- Ip SC, Borja RI (2023) Modeling heterogeneity and permeability evolution in a compaction band using a phase-field approach. *J Mech Phys Solids* 181:105441
- Kolawole O, Ispas I (2020) Interaction between hydraulic fractures and natural fractures: current status and prospective directions. *J Pet Explor Prod Technol* 10:1613–1634
- Kuhn C, Müller R (2010) A continuum phase field model for fracture. *Eng Fract Mech* 77:3625–3634
- Lecampion B (2009) An extended finite element method for hydraulic fracture problems. *Commun Numer Methods Eng* 25:121–133
- Lecampion B, Bungler A, Zhang X (2018) Numerical methods for hydraulic fracture propagation: a review of recent trends. *J Nat Gas Sci Eng* 49:66–83

33. Liu Z, Chen M, Zhang G (2014) Analysis of the influence of a natural fracture network on hydraulic fracture propagation in carbonate formations. *Rock Mech Rock Eng* 47:575–587
34. Lyu S, Wang S, Chen X, Wang S, Wang T, Shi X, Dong Q, Li J (2020) Natural fractures in soft coal seams and their effect on hydraulic fracture propagation: a field study. *J Petrol Sci Eng* 192:107255
35. Miehe C, Aldakheel F, Raina A (2016) Phase field modeling of ductile fracture at finite strains: a variational gradient-extended plasticity-damage theory. *Int J Plast* 84:1–32
36. Miehe C, Hofacker M, Welschinger F (2010) A phase field model for rate-independent crack propagation: robust algorithmic implementation based on operator splits. *Comput Methods Appl Mech Eng* 199:2765–2778
37. Mikelić A, Wheeler MF, Wick T (2015) Phase-field modeling of a fluid-driven fracture in a poroelastic medium. *Comput Geosci* 19:1171–1195
38. Morrow CA, Kaven JO, Moore DE, Lockner DA (2017) Physical properties of sidewall cores from Decatur, Illinois. US Department of the Interior, US Geological Survey
39. Nguyen VP, Lian H, Rabczuk T, Bordas S (2017) Modelling hydraulic fractures in porous media using flow cohesive interface elements. *Eng Geol* 225:68–82
40. Prajapati N, Herrmann C, Späth M, Schneider D, Selzer M, Nestler B (2020) Brittle anisotropic fracture propagation in quartz sandstone: insights from phase-field simulations. *Comput Geosci* 24:1361–1376
41. Shauer N, Duarte CA (2022) A three-dimensional generalized finite element method for simultaneous propagation of multiple hydraulic fractures from a wellbore. *Eng Fract Mech* 265:108360
42. Sonntag A, Wagner A, Ehlers W (2023) Dynamic hydraulic fracturing in partially saturated porous media. *Comput Methods Appl Mech Eng* 414:116121
43. Steeb H, Renner J (2019) Mechanics of poro-elastic media: a review with emphasis on foundational state variables. *Transp Porous Media* 130:437–461
44. Truesdell C, Toupin RA (1960) The classical field theories. In: Flügge S (ed) *Handbuch der Physik*, III(1). Springer, Berlin, pp 226–858
45. Wagner A, Eggenweiler E, Weinhardt F, Trivedi Z, Krach D, Lohrmann C, Jain K, Karadimitriou N, Bringedal C, Volland P, Holm C, Class H, Steeb H, Rybak I (2021) Permeability estimation of regular porous structures: a benchmark for comparison of methods. *Transp Porous Media* 138:1–23
46. Wagner A, Sonntag A, Reuschen S, Nowak W, Ehlers W (2023) Hydraulically induced fracturing in heterogeneous porous media using a TPM-phase-field model and geostatistics. *Proc Appl Math Mech* 23:e202200118
47. Yang JF, Ohji T, Kanzaki S, Díaz A, Hampshire S (2002) Microstructure and mechanical properties of silicon nitride ceramics with controlled porosity. *J Am Ceram Soc* 85(6):1512–1516
48. Yi L, Li X, Yang Z, Waisman H (2019) A fully coupled fluid flow and rock damage model for hydraulic fracture of porous media. *J Petrol Sci Eng* 178:814–828
49. Yi L, Li X, Yang Z, Yang C (2020) Phase field modeling of hydraulic fracturing in porous media formation with natural fracture. *Eng Fract Mech* 236:107206
50. Zhang F, Damjanac B, Maxwell S (2019) Investigating hydraulic fracturing complexity in naturally fractured rock masses using fully coupled multiscale numerical modeling. *Rock Mech Rock Eng* 52:5137–5160
51. Zheng H, Pu C, Sun C (2020) Study on the interaction between hydraulic fracture and natural fracture based on extended finite element method. *Eng Fract Mech* 230:106981

Publisher's Note Springer Nature remains neutral with regard to jurisdictional claims in published maps and institutional affiliations.